The pseudo-Voigt function is an approximation to the Voigt function, which is the convolution of a Gaussian and a Lorentzian:

Voigt function

$$P_V(\Delta, \Gamma_L, \Gamma_G) = \int_{-\infty}^{\infty} P_L(\Delta, \Gamma_l) P_G(\Delta - \delta, \Gamma_G)\, \mathrm{d}\delta = \left(\frac{4 \ln 2}{\pi \Gamma_G^2}\right)^{1/2} \mathrm{Re}[\exp(-z^2)\mathrm{erfc}(-iz)], \quad (3.3.9)$$

where $z = \alpha + i\beta$, $\alpha = (4 \ln 2)^{1/2} \Delta/\Gamma_G$ and $\beta = (\ln 2)^{1/2} \Gamma_L/\Gamma_G$.

A number of formulations have been proposed for the pseudo-Voigt coefficients to make the best fit to the corresponding Voigt function (Hastings *et al.*, 1984; David, 1986; Thompson *et al.*, 1987). The latter is most commonly used and gives overall the FWHM, Γ and the mixing coefficient, η, to be used in equation (3.3.8) as functions of the individual FWHMs Γ_G and Γ_L:

$$\Gamma = [(\Gamma_G^5 + 2.69269\Gamma_G^4\Gamma_L + 2.42843\Gamma_G^3\Gamma_L^2 + 4.47163\Gamma_G^2\Gamma_L^3 + 0.07842\Gamma_G\Gamma_L^4 + \Gamma_L^5)]^{1/5}, \quad (3.3.10)$$

$$\eta = 1.36603(\Gamma_L/\Gamma) - 0.47719(\Gamma_L/\Gamma)^2 + 0.11116(\Gamma_L/\Gamma)^3. \quad (3.3.11)$$

The alternative given by David (1986) uses a more generalized version of the pseudo-Voigt function,

$$\begin{aligned} P_{\mathrm{PV}}(\Delta, W_G, W_L, \eta_G, \eta_L) &= \eta_L P_L(\Delta, W_L) + \eta_G P_G(\Delta, W_G), \\ \eta_G &= 0.00268\rho_1 + 0.75458\rho_1^2 + 2.88898\rho_1^3 - 3.85144\rho_1^4 \\ &\quad - 0.55765\rho_1^5 + 3.03824\rho_1^6 - 1.27539\rho_1^7, \\ \eta_L &= 1.35248\rho_2 + 0.41168\rho_2^2 - 2.18731\rho_2^3 + 6.42452\rho_2^4 \\ &\quad - 10.29036\rho_2^5 + 6.88093\rho_2^6 - 1.59194\rho_2^7, \\ W_G &= \Gamma(1 - 0.50734\rho_2 - 0.22744\rho_2^2 + 1.63804\rho_2^3 \\ &\quad - 2.28532\rho_2^4 + 1.31943\rho_2^5), \\ W_L &= \Gamma(1 - 0.99725\rho_1 + 1.14594\rho_1^2 + 2.56150\rho_1^3 \\ &\quad - 6.52088\rho_1^4 + 5.82647\rho_1^5 - 1.91086\rho_1^6), \end{aligned} \quad (3.3.12)$$

where $\Gamma = \Gamma_G + \Gamma_L$, $\rho_1 = \Gamma_G/\Gamma$ and $\rho_2 = \Gamma_L/\Gamma$; this is claimed to match the Voigt function to better than 0.3%.

3.3.2.2. *Constant-wavelength powder profile asymmetry*

Rietveld (1969) noted that at very low scattering angles the peaks displayed some asymmetry, which shifted the peak maximum to lower angles. He ascribed the effect to 'vertical divergence' and proposed a purely empirical correction for it. Subsequent authors (Cooper & Sayer, 1975; Howard, 1982; Hastings *et al.*, 1984) offered semi-empirical treatments of the profile shape that results from the intersection of a Debye–Scherrer cone with a finite receiving slit, which is described as 'axial divergence'. A more complete analysis of the problem in neutron powder diffraction was offered by van Laar & Yelon (1984), who considered the effect of a finite vertical slit ($2H$) intercepting a set of Bragg diffraction cones generated from a finite sample length ($2S$) within the incident beam for a goniometer radius (L). As seen in Fig. 3.3.1, this gives peak intensity beginning at $2\varphi_{\min} < 2\theta$ *via* scattering from only the ends of the sample; at $2\varphi_{\mathrm{infl}}$ the entire sample scatters into the detector. The resulting intensity profile is then convoluted with a Gaussian function to give the resulting asymmetric powder line profile (Fig. 3.3.2). This approach was then considered by Finger *et al.* (1994) for synchrotron powder diffraction and they created a Fortran code that was subsequently adopted *via* convolution with a pseudo-Voigt function [equation (3.3.12)] for use by many Rietveld refinement codes. Although originally formulated for parallel-beam neutron optics, it was shown by Finger *et al.* (1994) that it could be equally well applied to diverging X-ray and neutron optics by allowing the sample length to vary during the Rietveld refinement. They also showed that it could be applied to the asymmetry observed at low angles with Bragg–Brentano instrumentation. In that case the detector height is defined by the diffracted-beam Soller slits.

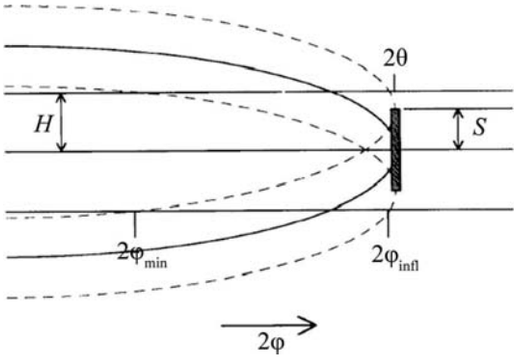

Figure 3.3.1
The band of intensity diffracted by a sample with height $2S$, as seen by a detector with opening $2H$ and a detector angle 2φ moving in the detector cylinder. For angles below $2\varphi_{\min}$ no intensity is seen. For angles between $2\varphi_{\mathrm{infl}}$ and 2θ, scattering from the entire sample can be seen by the detector. Figure and caption adapted from Finger *et al.* (1994).

Clearly, this asymmetric peak-shape function properly represents the offset of the peak top from the peak position, in contrast to functions such as the split Pearson VII function. Consequently, single peak fits using this function will give peak positions that are more readily indexed using methods such as those described in Chapter 3.4.

3.3.2.3. *Peak-displacement effects*

The position of the peak is also affected by various instrumental and geometric effects. For example, the sample position in a Bragg–Brentano experiment is ideally tangent to the focusing circle (Parrish, 1992). A radial displacement, s, of the sample will shift the Bragg peaks according to

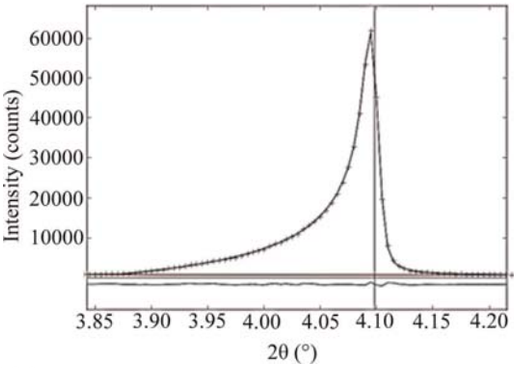

Figure 3.3.2
Low-angle synchrotron powder diffraction line ($2\theta \simeq 4.1^\circ$) fitted by the Finger *et al.* (1994) axial divergence powder line-shape function. The observed points (+), calculated curve, background and difference curves are shown. Note the offset of the peak top from the Bragg 2θ position (vertical line).

$$\Delta 2\theta = 360 s \cos\theta / \pi R, \tag{3.3.13}$$

where R is the goniometer radius. This is the major peak-displacement effect and can be detected for sample displacements as small as 10 μm.

A similar effect can be observed for Debye–Scherrer instrumentation when the goniometer axis is not coincident with the sample axis; this is a more common problem for neutron powder diffraction instruments where accurate placement of very massive goniometers can be difficult. In this case the peak displacement is

$$\Delta 2\theta = \frac{180}{\pi R}(s_x \cos 2\theta + s_y \sin 2\theta), \tag{3.3.14}$$

where s_x and s_y are displacements perpendicular and parallel to the incident beam, respectively, all in the diffraction plane.

In high-resolution instrumentation (even at a synchrotron) goniometer axis displacements less than 10 μm can be detected.

Specimen transparency in Bragg–Brentano diffraction can also cause peak displacements arising from the shift in effective sample position to below the surface at high scattering angles. This shift for a thick specimen is

$$\Delta 2\theta = 90 \sin 2\theta / \mu_{\rm eff} \pi R, \tag{3.3.15}$$

where $\mu_{\rm eff}$ is the effective sample absorption coefficient taking into account the packing density.

3.3.2.4. *Fundamental parameters profile modelling*

An alternative method for describing the source and instrumental part of the powder peak profile is to develop a set of individual functions that form the part of the profile arising from each of the instrumental components that shape the beam profile (Cheary & Coelho, 1992, 1998*a*,*b*). Ideally, each function is parameterized in terms of the physical parameters of the corresponding instrument component (*e.g.* slit width and height, sample dimensions and absorption, source size and emission characteristics, *etc.*), which are known from direct measurement. The set of functions are then convoluted *via* fast mathematical procedures to produce a line profile that matches the observed one. Any remaining profile-broadening parameters (*e.g.* for sample crystallite size and microstrain, see Section 3.3.5 for details) are then allowed to adjust during a Rietveld refinement. By employing this fundamental parameters (FP) approach, these parameters are unaffected by any instrumental parameterization.

The FP method offers two clear advantages over the more empirical approach outlined in Sections 3.3.2.1–3.3.2.3 above: (i) it can more closely describe the actual instrumental effects that contribute to the profile shape, thus improving the precision of the fit to the observed data and (ii) it can be used to describe a source characteristic or an instrumental arrangement that is outside the normally used configuration, yielding a result that would be difficult to obtain otherwise (Cheary *et al.*, 2004).

3.3.3. Peak profiles for neutron time-of-flight experiments

3.3.3.1. *The experiment*

The neutron source in a time-of-flight (TOF) powder diffraction experiment produces pulses of polychromatic neutrons; these travel over the distance from the source to the sample and then to the detectors which are placed at fixed scattering angles about the sample position; the travel times are of the order of 1–100 ms. This has been briefly described in Volume C of *International Tables for Crystallography* (Jorgensen *et al.*, 1992). Because neutrons of differing velocities (v) have differing wavelengths (λ) according to the de Broglie relationship ($\lambda = h/mv$) given Planck's constant (h) and the neutron mass (m), they will sort themselves out in their time of arrival at the detector. The powder pattern appears as a function of TOF *via* Bragg's law ($\lambda = 2d\sin\theta$) in which the wavelength is varied and θ is fixed. The approximate relationship between TOF, wavelength and d-spacing observed in a particular detector can be derived from the de Broglie relationship and Bragg's law to give

$$\mathrm{TOF} = 252.7784 L\lambda = 505.5568 L d \sin\theta. \tag{3.3.16}$$

The constants are such that given λ in ångströms and the total neutron flight path length L in metres, then the TOF will be in μs. An analysis of the possible variances in these components then gives an estimate of the powder diffraction peak widths:

$$\Delta d/d = [(\Delta t/t)^2 + (\Delta\theta \cot\theta)^2 + (\Delta L/L)^2]^{1/2}, \tag{3.3.17}$$

where Δd, Δt, $\Delta\theta$ and ΔL are, respectively, the uncertainties in d-spacing, TOF, scattering angle θ and total flight path L (Jorgensen & Rotella, 1982). Consequently, these three terms also determine the instrumental contribution to the neutron TOF powder peak profile.

3.3.3.2. *The neutron pulse shape*

The neutron pulse shape depends on the mode of production. Early studies (Buras & Holas, 1968; Turberfield, 1970) used one or more choppers to define a polychromatic pulse from a reactor source, resulting in essentially Gaussian powder peak profiles whose FWHM (Γ_G) is nearly constant ($B \simeq 0$):

$$\Gamma_G^2 = A + Bd^2, \tag{3.3.18}$$

so that the Rietveld technique can easily be used (*e.g.* Worlton *et al.*, 1976). Unfortunately, this approach gave very low intensities and relatively low resolution powder patterns.

A more useful approach uses a spallation source to produce the pulsed neutron beam. Neutrons are produced when a high-energy proton beam (>500 MeV) strikes a heavy metal target (usually W, U or liquid Hg) *via* a spallation process (Carpenter *et al.*, 1984). These very high energy neutrons strike small containers of moderating material (usually H_2O, liquid CH_4 or liquid H_2) which then comprise the neutron source seen by the powder diffraction instrument. The entire target/moderator system is encased in a neutron-reflective material (usually Be) to enhance the neutron flux and then further encased in a biological shield. Each moderator may be encased on the sides away from the instrument (*e.g.* powder diffractometer) in a thin neutron absorber (*e.g.* Cd or Gd) and may also contain an inner absorber layer ('poison') to sharpen the resulting pulse of thermal neutrons. These sources produce a polychromatic neutron beam that is rich in both thermal (<300 meV) and epithermal (>300 meV) neutrons. The proton pulses can have a very short duration (~200 ns) (from a 'short-pulse' source, *e.g.* ISIS, Rutherford Laboratory, UK or LANSCE, Los Alamos National Laboratory, USA) or a much longer duration (>500 ns) (a 'long-pulse' source, *e.g.* SNS, Oak Ridge National Laboratory, USA or ESS, European Spallation Source, Sweden); the pulse repetition rate at these sources is 10–60 Hz. These characteristics are largely dictated by the proton accelerator and neutron source design. The resulting neutron pulse results from complex down-scattering and thermalization processes in the whole target/moderator assembly; it may be further shaped by choppers,